High performance triboelectric nanogenerators based on phase-inversion piezoelectric membranes of poly(vinylidene fluoride)-zinc stannate (PVDF-$ZnSnO_3$) and polyamide-6 (PA6)

High performance triboelectric nanogenerators based on phase-inversion piezoelectric membranes of poly(vinylidene fluoride)-zinc stannate (PVDF-$ZnSnO_3$) and polyamide-6 (PA6)

Navneet Soin,[a,†] Pengfei Zhao,[a,†] Kovur Prashanthi,[b] Jinkai Chen,[c] Peng Ding,[c] Erping Zhou,[a] Tahir Shah,[a] Sekhar C. Ray,[d] Christos Tsonos[e], Thomas Thundat,[b] Elias Siores,[a] and Jikui Luo[a,c,*]

[a]Institute for Materials Research and Innovation (IMRI), University of Bolton, Deane Road, Bolton, BL3 5AB, United Kingdom.

[b]Ingenuity Lab, Department of Chemical and Materials Engineering, University of Alberta, Edmonton, Alberta, T6G 2V4, Canada

[c]Department of Information Science & Electrical Engineering, Zhejiang University, 38 Zheda Road, Hangzhou 310027, P. R. China

[d]Department of Physics, College of Science, Engineering and Technology, University of South Africa, Private Bag X6, Florida, 1710, Science Campus, Christiaan de Wet and Pioneer Avenue, Florida Park, Johannesburg, South Africa

[e]Electronics Engineering Department, Technological Educational Institute (TEI) of Sterea Ellada, 35100 Lamia, Greece

†These authors contributed equally to the work.

*Corresponding Author: Prof. Jikui Luo, Email: j.luo@bolton.ac.uk

Abstract

Vertical contact-separation mode triboelectric generator (TEG) based on lead-free perovskite, zinc stannate ($ZnSnO_3$)-polyvinylidene fluoride (PVDF) composite and polyamide-6 (PA6) membrane is demonstrated. For the 5wt% PVDF-$ZnSnO_3$ nanocomposites, the facile phase-inversion method provides a simple route to achieve high crystallinity and β-phase with a piezoelectric coefficient d_{33} of -65 pmV^{-1}, as compared to -44 pmV^{-1} for pristine PVDF membranes. Consequently, at a cyclic excitation impact of 490 N/3 Hz, the PVDF-$ZnSnO_3$/PA6 based TEGs provide a significantly higher voltage of 520 V and a current

density of 2.7 mAm^{-2} (corresponding charge density of 62.0 μCm^{-2}), as compared to the pristine PVDF-PA6 TEG which provides up to 300 V with a current density of 0.91 mAm^{-2} (corresponding to a charge density of 55.0 μCm^{-2}). This increase in the electrical output can be attributed to not only the enhanced polarisation of PVDF by $ZnSnO_3$ leading to an increase in the β-phase content, but also to the surface charge density increase by stress induced polarisation of $ZnSnO_3$, leading to the generation of stronger piezoelectric potential. The work thus introduces a novel method of enhancing the surface charge density *via* the addition of suitable high polarization piezoelectric materials thus eliminating the need for prior charge injection for fluoropolymer membranes.

Keywords: Polyvinylidene fluoride (PVDF); Zinc Stannate ($ZnSnO_3$); Polyamide-6 (PA6); β-phase; Triboelectric Nanogenerator

1. Introduction

With the rapid advances in wearable and wireless electronic devices, the need for high performance energy harvesters to scavenge electrical power from ambient sources as well as human movement to power electronic devices is becoming hugely important [1-3]. To this effect, triboelectric generators (TEG) have gained huge attention due to their high energy output and conversion efficiency, ease of fabrication, simple design and use of inexpensive materials [4-6]. The TEG operation is based on the contact electrification and electrostatic phenomena in which the static charges are produced on the dissimilar dielectric polymer surfaces when they are brought into contact with each other [5, 6]. The triboelectric charge density itself can be improved by judicious selection of the materials, i.e. the materials chosen should be as far apart in the triboelectric series in their ability to gain/loss charges [6-8]. By observing the triboelectric series, it is clear that polyamide-6 (PA6, Nylon) tends to lose electrons when it is in contact with other polymers while poly(vinylidene fluoride), PVDF, has a significant ability to gain electrons owing to the large electronegativity of the fluorine groups. To this effect, TEGs based on fluorinated polymers and polyamides have been shown in the literature for energy harvesting systems, self-powered anti-corrosion system and UV detectors among other applications [9-11]. Further enhancement in the charge density of such systems can be obtained by modulation of surface roughness by plasma

treatment [12], silicon nanostructures based templating [13], ion beam etching [14], biomimetic structures [15], nanoparticle dispersion [16] and more recently through ferroelectric polarisation mediation [17]. For fluorinated polymers, the charge density can be enhanced via controlling the polarisation state by either using external electric field or via the use of suitable additives and processes to yield high polarisation. In a recent study carried out by Lee et al. [18], it was observed that for a pristine poly[(vinylidenefluoride-co-trifluoroethylene] - polyethylene napthalte based TEG, post-polarisation of PVDF enhanced the output voltage from an initial value of 15 V to 400 V. To induce and enhance the polarised β-phase in PVDF based systems, high electric fields of ~100 MV/m or above are required under elevated temperatures (>80-90 °C), which is time consuming procedures and needs expensive high voltage setups. In our recent work [19], we have demonstrated self-polarised PVDF films via a facile phase-inversion technique wherein the polymorphism of the films was controlled from an exclusive α-phase (>90%) to β-phase (>95%) by simply varying the quenching temperature of the films, thereby making them highly suitable for electroactive applications.

As one of many Pb-free piezoelectric materials in non-centrosymmetric group, zinc stannate ($ZnSnO_3$), shows a strong piezoelectric response and a large spontaneous polarization value [20]. This large polarisation value occurs due to the large displacement of Zn based on a strong covalent bond between three oxygen and zinc atoms [21] and is significantly higher than other oxides such as $KNbO_3$, ZnO and $BaTiO_3$. As a relatively new material, $ZnSnO_3$ is widely desired to be utilized in piezoelectric application for nanogenerators in various structure with high polarization, for example $ZnSnO_3$ with $LiNbO_3$ (LN)-type structure [20], synthesized upon high pressurization or ilmenite-type $ZnSnO_3$ [22] synthesized by an ion exchange method. More recently, piezoelectric nanocomposites generators based on PDMS with an enclosure of $ZnSnO_3$ of 6-40 wt% have been reported in the literature [23]. In a recent report by Wang et al. [23], TEG based on 6 wt% PDMS-$ZnSnO_3$/aluminium system produced 400 V and 28 μA with an effective power of 3 mW, demonstrated its potential for the development of high performance generator. Herein, based on the enhanced triboelectrificaton of dielectric PVDF-$ZnSnO_3$ composite membranes; PVDF-$ZnSnO_3$/PA6 triboelectric generators are demonstrated. The membranes were synthesised using a facile phase-inversion method which provides a simple route to control and achieve high crystallinity and β-phase for the PVDF and PVDF-$ZnSnO_3$ membranes. Under the vertical contact mode, the voltage and current outputs for PVDF-$ZnSnO_3$/PA6

system are enhanced by 70 and 200%, respectively. Through a further optimisation of spacing between the membranes, peak-to-peak open-circuit voltage (V_{oc}) of 1200 V and short-circuit current (I_{sc}) of 20 μA can be achieved. The increase in the power output of the PVDF-$ZnSnO_3$/PA6 system is attributed to the enhanced polarisation and β-phase content and crystallinity of the PVDF/$ZnSnO_3$ membranes. The work thus introduces a simple route for enhancing the polarisation and power output of TEGs without relying on prior charge injection technique and thus has the potential to be utilised further to making self-powered systems.

2. Experimental

2.1 Materials

Polaymide-6 (TECHNYL 1011R) was obtained from Rhodia Ltd.; PVDF (SOLEF 1006) from Solvay Solexis Ltd. and $ZnSnO_3$ nanocube powders (FLAMTARD S, approximate size of 400-500 nm, see Supporting Information, S1) from William Blythe Ltd. (U.K.). To ensure homogeneous distribution of $ZnSnO_3$ (5wt%) in the PVDF matrix, the composites were prepared using Thermoelectron Prism Eurolab 16 twin screw extruder with a 16 mm screw diameter and a L/D value of 24. The PVDF homopolymer has a melt flow index of 40g/10min at 230 ^oC and 2.16 kg mass with the melting point and crystallisation temperature of ~175 ^oC and 138 ^oC, respectively. The temperature profile set during the compounding process was: 150 (hopper-end), 200, 205, 205, 200, and 200 °C (die head) with a screw speed of 350 rpm. The compounded samples were extruded as single strands of ~2 mm diameter into a water bath before passing through a pelletiser to obtain PVDF-$ZnSnO_3$ composites. The high shear speeds encountered during the compounding process helps achieve high dispersion of $ZnSnO_3$ in the PVDF matrix.

2.2 Membrane Preparation by phase-inversion process

The dope solutions for the synthesis of the membranes was prepared using a 20 wt% solution in the corresponding solvent (Formic acid for PA6 and *N, N*-Dimethylformamide for PVDF, respectively) by continuously stirring at approximately 70 °C for three hours. After the preparation of dope solution, a certain volume of the solution was deposited on highly polished silicon wafer *via* spin-coating process. The spin-coating process was performed using Spin 150 single substrate spin processor using the following protocol: initial spinning at

10 rpm (rotation per minute) for 5 sec followed by 2000 rpm for 20 sec. The coated substrate was then immersed immediately in an anti-solvent bath kept at the desired quenching temperature, T_Q, of ~20 ^oC. The free-standing membranes thus obtained were then rinsed repeatedly in distilled water and left overnight in de-ionised water to remove any residual solvent. The complete removal of solvent was further confirmed through Fourier transform infrared spectroscopy (FTIR) analysis.

2.3 Preparation of triboelectric generators

The double-layered structure of the TEG is shown in Fig. 1 wherein the first layer of PA6 membrane is attached using a conductive adhesive aluminium tape electrode on one side, while the opposite side is of PVDF or PVDF-$ZnSnO_3$ blend membrane, again attached using conductive aluminium tape. The diameters of all three different types of circular membranes were 8.5 cm. Two square acrylic sheets of 9 cm x 9 cm were used as the substrate and each of the membranes was fixed on its centre. These two substrates were then connected using two arc-shaped polyimide supports to maintain the desired spacing between them.

2.4 Characterisation

A Hitachi S3400N scanning electron microscope (SEM) was used to characterise the microstructure of the membranes. The vibrational characteristics of the films were examined by FTIR spectroscopy (Thermo Scientific IS10 Nicolet). Vendor provided OMINIC software was used to analyse the results, including the calculation of β-phase content. The spectra were recorded at a nominal resolution of ±1 cm^{-1} for a total of 64 scans. Differential scanning calorimetry (DSC) was used to investigate the crystalline phase of the polymer films on a TA Instruments DSC Q2000. The samples, approximate weight of 2 mg, were heated at 5 $^oCmin^{-1}$ from -50 to 200 ^oC under 50 $ml.min^{-1}$ N_2 flow. Dielectric properties of the samples were studied by Dielectric Relaxation Spectroscopy (DRS) technique using Alpha analyzer. Gold electrodes were sputtered (using a sputter coater EMS 550) on both sides of the samples to ensure good electrical contact between the sample and the gold-plated capacitor plates. The complex dielectric permittivity was recorded and measured in a broad frequency ranged from 0.01 to 10^6 Hz.

The electric field mapping and piezoelectric response of pristine PVDF and PVDF-$ZnSnO_3$ blend membranes were investigated using electric force microscopy (EFM) and

piezoresponse microscopy (PFM) modes on a Bruker Icon AFM (Santa Barbara, CA) system. In the two-step EFM mode, the topographic image was obtained during the main scan in the tapping mode. During interleave (lift) mode, the tip was raised above the sample surface allowing the imaging of relatively weak but long-range electrostatic interactions while minimizing the influence of topography. For PFM imaging, a drive voltage of 5 V (for PVDF sample) and 10 V (for PVDF-$ZnSnO_3$ sample) was used. For both EFM and PFM imaging, we have used electrically conducting (Pt/Ir coated) SCM-PIT probe with a resonance frequency of 64 kHz and spring constant of 2.8 N/m. The images were processed and analysed using Nanoscope analysis software (V1.40, Bruker).

The electrical measurements of the TEG were carried out using an Instron 8872 fatigue testing system in conjunction with a TDS3012B oscilloscope and Keithley picoammeter. The operating load and speed range of the fatigue testing system are between 2 to 25,000 N and 0.005 to 60,000 $mm.min^{-1}$ thus allowing relatively precise control over the impact load and frequency. In addition, the system allows the collection of the impact force data during high speed operation, thus the impact force when two layers of the TEGs make a direct contact can be directly detected by the system during the test.

3. Results and discussion

3.1 Microstructural characterisation of phase-inversion membranes

During the phase inversion process, the PVDF and PVDF-$ZnSnO_3$ membranes are formed by quenching the spin coated films into a non-solvent bath to induce rapid liquid–liquid and liquid–solid phase separation events [19, 24, 25]. The microstructure and crystalline phase of the resulting films are a complex function of the experimental parameters of composition (wt%), solvent-type, anti-solvent and quenching temperature etc. Figs. 2 (a-f) shows the surface and the cross-sectional structure of the PVDF, PVDF-$ZnSnO_3$ and PA6 membranes. In our previous work [19], we have shown that the porosity of the PVDF membranes decreases with the decrease in the T_Q which is attributed to the slow crystallisation and elimination of DMF from the dope solution which itself arises from the reduced mobility and miscibility of DMF at lower temperatures. For both PVDF and PVDF-$ZnSnO_3$ membranes, it can be clearly observed that the porous structure exists only on the surface of the membranes rather than throughout the cross-section. In fact, the diameter of the pores on the pristine PVDF membrane is in the range from 0.1-0.5 μm, whereas the pores on PVDF-$ZnSnO_3$

membranes are in the 0.5-1.0 μm range with a slightly higher density, which could be attributed to the changes in liquid-solid phase separation events due to the presence of second phase i.e. $ZnSnO_3$. The presence of $ZnSnO_3$ in the composite membranes was confirmed using X-ray photoelectron spectroscopy (see Supporting Information, S2). As compared to the PVDF membranes (5-10 μm), the slightly thicker PA6 membranes (~20 μm) shows significantly higher porosity with a pore size of 1.0-1.5 μm which again does not extend throughout the thickness of the membrane. According to previous studies, porosity can be introduced into the PA6 membrane structure via the addition of water into the PA6/formic acid dope solution and further enhanced by increasing the concentration of water in the system [26, 27]. While no water was introduced separately during the membrane formation process, the ability of polyamides to absorb water from the ambient quite readily and the fact that there is nearly 2.5% water in the formic acid itself would have contributed to the introduction of porosity in the membranes [26, 27]. For both the PVDF and PA6 membranes, the rapid removal of solvent arising due to the solvent anti-solvent interaction leads to the formation of porosity in the structure which can contribute positively to the enhancement in the power density of the TEGs. Previous studies carried out by various groups have demonstrated that the charge density of the TEG can be enhanced by effectively controlling the microstructure and porosity of the polymer films [4, 9, 28, 29]. In a recent work by Wang et al., nanostructured porous PVDF and PA6 membrane based TEG produced a significantly higher charge density (71 μCm^{-2}) than their smooth counterpart (48 μCm^{-2}), on account of larger surface area, thus showing the effect of porosity on the TEG operation and as such is a contributory factor in enhancing the power output of the TEG [9].

The Fourier transform infrared spectroscopy (FTIR) of the PVDF and PVDF-$ZnSnO_3$ films is shown in Fig. 3(a). The quantification of the β-phase in crystalline PVDF matrix relative to α-phase was carried out using the signature vibrational bands at 760 cm^{-1} (CF_2 bending and skeletal bending) and 840 cm^{-1} (CH_2 rocking and CF_2 asymmetric stretching vibration) [19, 30-36]. Upon phase inversion, a significant increase in the β-phase is achieved for the PVDF membranes, wherein the β-phase is enhanced to ~49% from an initial value of from ~35% for the starting PVDF pellets. With the introduction of $ZnSnO_3$ to the PVDF, at the same processing conditions, the β-phase content is further enhanced to nearly 72%. Interfacial interactions occurring between the $ZnSnO_3$ nanocubes and the PVDF matrix were also observed *via* the shifts in the CH_2 asymmetric and symmetric stretching vibrations modes as shown in Fig. 3(b). For the PVDF-$ZnSnO_3$ membranes, as compared to both

pristine PVDF pellets and membranes, the asymmetric CH_2 (υ_{as}) vibrations showed a marked downshift from ~3025 cm^{-1} to ~3019 cm^{-1}, which has been attributed to the increase in the effective mass of the CH_2 dipoles resulting in the damping of the vibrational frequency [37, 38]. In fact, the deconvoluted values of the FTIR peak positions match very well with those reported in the literature for the β-phase PVDF films, wherein the calculated frequencies for the weak asymmetrical and symmetrical peaks occur at 3024 and 2984 cm^{-1}, respectively [39] (see Supporting Information, S3). A similar shift in the XPS spectra of the PVDF-$ZnSnO_3$ membranes was observed CH_2 binding energy wherein its peak position shifted by 0.7 eV (Fig. 3(c)) along with a corresponding increase in the density of states observed from the ultra-violet photoelectron spectroscopy (UPS) measurements (see Supporting Information, S4).

The positive effect of adding $ZnSnO_3$ to obtain enhanced crystallization of PVDF in the β-phase is further corroborated by the Differential Scanning Calorimetry (DSC) results. For the DSC thermograms shown in Fig. 3(d), unlike the PVDF pellets, both the PVDF and PVDF-$ZnSnO_3$ membrane samples show shoulder-like structures around the main melting peak with changes observed in the melting temperature, T_M, as well. It is largely accepted in the literature that β-phase crystallite melting occurs in the range 165–172 ^oC; α-phase in the range 172–175 ^oC with the γ-phase melting between 175 and 180 ^oC (marked in Fig. 3(d)) [19, 24, 25, 34, 35]. The T_M of PVDF granules and pristine PVDF membranes is 173.6 °C and 173.0 °C respectively, very close to each other. However, the T_M of PVDF-$ZnSnO_3$ membrane is 165.5 °C, approximately 8 °C lower than the other two samples. According to the previous reports, this reduction of the T_M is largely caused by the enhanced β-phase content and the change in the porosity of the membranes [19, 32, 36]. For starting pellets, a low crystallinity of the order of 38.6% is observed which is enhanced to nearly 46.8% for the pristine PVDF membranes and is further enhanced to nearly 60.1% for the PVDF-$ZnSnO_3$ membranes (Fig. 3(e)). These values are in agreement with those obtained from FTIR measurements shown above. From previous studies carried out by Gomes et al. [33], for PVDF it has been established that the piezo- and ferro-electric behaviour of PVDF depends on the crystalline β-phase content and the saturation polarization increases with an increase in the ferroelectric β-phase content in the sample. The PVDF-$ZnSnO_3$ membranes with higher β-phase content should display higher polarization and as such should possess larger triboelectric charge density for acquiring the electrons from the PA6 membrane. As compared to the PVDF membranes, the PVDF-$ZnSnO_3$ membranes show an increase in the

real part of the complex dielectric permittivity, ε` across the measurement range (Fig. 3(f)) which should correspond to higher polarisation. Due to the lower loading of $ZnSnO_3$ (5 wt%, ~2.5 vol%), no interfacial or Maxwell-Wagner Sillars (MWS) polarisation could be observed, however an increase in the dielectric constant of the composite membranes was still notable, particularly in the low frequency range [29, 30]. For polymer systems, it is understood that the higher dielectric constant can also arise from the lower crystallinity of the samples as the chains are more mobile, however the DSC results show significantly higher crystallinity for the composite samples, thus confirming that enhancement of ε` comes from the presence of $ZnSnO_3$.

3.2 Electrical characterisations of TEGs

Figs. 4(a, b) shows the output voltage of pristine PVDF/PA6 and PVDF-$ZnSnO_3$/PA6 TEGs with three different spacer distances (5 cm, 10 cm, and 15 cm) at a fixed driving frequency of 3 Hz. At the same working frequency, with the increase in the spacing between the two substrates, the force value detected by the sensor at the precise moment of contact between the two layers also increases. It can be clearly observed that the magnitude of the output voltage increases almost linearly as a function of the applied force (spacing). In fact, at 140 N/5 mm gap spacing, the output voltage detected from the PVDF-$ZnSnO_3$/PA6 TEG (242 V) was nearly 2.5 times higher than the pristine PVDF/PA6 TEG (90 V). This increasing trend continues across the force, spacing variables with a maximum voltage value of 254 V and 378 V for the PVDF/PA6 TEG and PVDF-$ZnSnO_3$/PA6 TEG, respectively (Fig. 4(c)). It should be mentioned that while both the V_{oc} and I_{sc} are dependent on the triboelectric charge density (σ) and constitute as vital parameters to understand the behaviour of the TEG; V_{oc} is affected by the charge density (σ) and some controllable effects, such as spacer distance (d), whereas the I_{sc} is further dependent on the contact speed as well [40, 41]. Thus, for assessing the device characteristics, it is often easier to compare the V_{oc} values especially if the other test parameters such as contact speed cannot be fully controlled. By looking at the current density values given in Fig. 4(e), it is quite obvious that the peak current output for PVDF/$ZnSnO_3$ TEG seems relatively unstable. At the working condition of 140 N/5 mm, the PVDF and PVDF-$ZnSnO_3$ TEGs supplied peak current (peak current densities) of 1.3 μA (0.23 mAm^{-2}) and 4.6 μA (0.80 mAm^{-2}), respectively, corresponding to a charge density of 30.2 μCm^{-2} and 52.9 μCm^{-2}. The values obtained from these systems are very similar to those obtained from nanostructured PVDF/PA6 system [9]. The rather

unstable values obtained for the transitionary values of 290 N/10 mm can be explained by invoking the stress/strain induced polarisation effects in $ZnSnO_3$ nanocubes. It has been reported previously for $ZnSnO_3$ based piezo/triboelectric systems, below a certain stress/strain threshold, no significant enhancement in the electrical output was observed. However, once this value was exceeded, the higher stress values being applied to the system and hence to the $ZnSnO_3$ nanocubes embedded inside the PVDF matrix, results in the generation of stronger piezoelectric potential and higher charge density from the PVDF-$ZnSnO_3$ system [23, 42, 43]. Indeed, at still higher stress values of 489 N, the stress induced alignment ensures that much more stable current output is obtained for PVDF-$ZnSnO_3$ TEG. In fact, the respective values for PVDF and PVDF-$ZnSnO_3$ TEG were 5.5 µA (55.2 μCm^{-2}) and 15.2 µA (62.0 μCm^{-2}), respectively corresponding to a current density of 0.91 mAm^{-2} and 2.7 mAm^{-2}, respectively. Thus, under the same working conditions, performance parameters of V_{oc}, I_{sc} and charge density of PVDF-$ZnSnO_3$/PA6 TEG are all significantly better than the pristine PVDF/PA6 TEG, indicating that the blend of $ZnSnO_3$ with PVDF contributed to the improvement of the output performance of TEG.

In order to determine the influence of impact frequency to the output of TEG, the output performance of PVDF-$ZnSnO_3$/PA6 TEG was tested under 1-7 Hz working frequency (Fig. 5 (a, b)). It should be mentioned that the applied force increased as a function of the frequency and increased from 90 N for 1 Hz frequency to nearly 730 N for 7 Hz frequency, as measured by the force sensor which monitored the impact when two layers of materials contacted each other. It is obvious that the output values are directly proportional to the frequency (impact force) wherein the V_{oc} increased from approximately 40 V to over 275 V with the corresponding I_{sc} values of 0.5 µA to 7 µA, corresponding to a charge density of 10 μCm^{-2} to nearly 150 μCm^{-2}.

Similarly, the electrical output from PVDF-$ZnSnO_3$/PA6 TEG was measured at a fixed frequency (3 Hz) while changing the spacer distance between them from zero to nearly 20 mm. The test with zero spacer between the membranes is to clarify whether the piezoelectric effect is responsible for the power generation or not as the force is directly applied to the sample with no triboelectric effect. Although small gaps between the two membranes and elastic properties of the membranes may contribute to the TEG effect, the output of the generator is mostly from piezoelectric effect. As it can be seen that the output voltage is less than 3 V, thus the majority of the power generated by the TEG is indeed through the triboelectric effect. Theoretically, the electric output from TEG should only be visible in the

process when two dissimilar dielectric materials either start to approach or separate from each other, while the piezoelectric effect should be observable when a complete contact of the two layers is achieved and a mechanical stress is applied consequently. As shown in Fig. 5(c), when the spacer between the two layers of the PVDF-$ZnSnO_3$/PA6TEG was completely removed, the output voltage was reduced drastically; however, a signal of approximately 3 V was still observed with phase-inversion symmetry caused due to its piezoelectric nature. However, it was observed that with a change in the spacer distance, the force measured by the sensor when the two materials actually come into contact is dramatically influenced by the spacer distance and as such cannot be controlled precisely. Furthermore, by modulating the spacing between the dielectric layers to 20 mm, the PVDF-$ZnSnO_3$/PA6 TEG can provide a peak-to-peak voltage of nearly 1200 V. From the Fig. S5 (Supporting Information), it can be clearly observed that the V_{oc} is also proportional to the force applied on the TEG. Thus, both the variation of working frequency and spacer distance illustrate that the electric output of PVDF-$ZnSnO_3$/PA6 TEG device is strongly dependent on the impact force used to drive the TEG.

According to previous studies [40], the V–Q–x relationship for the contact-mode TEG can be given by the following equation:

$$V = \frac{Q}{S\varepsilon_0} \times (d_0 + x) + \frac{\sigma x}{\varepsilon_0} \quad (1)$$

where Q is the amount of the transferred charge, S is the area size of the metal electrodes, x is the separation (spacer) distance between two charged layers, σ is the charge density of the inner surface of two triboelectric layers and ε_0 is the vacuum permittivity. For dielectric-to-dielectric TEG, the d_0 can be expressed as

$$d_0 = \frac{d_1}{\varepsilon_1} + \frac{d_2}{\varepsilon_1} \quad (2)$$

where d_1 and d_2 are the thickness of the PA6 and PVDF-$ZnSnO_3$ membranes, respectively and the ε_{r1} and ε_{r2} refer to the relative permittivity of PA6 and PVDF-$ZnSnO_3$, respectively. Since the values were test at open-circuit condition, no charge transfer occurs between the two electrodes, which means the value of Q can be considered as 0. Therefore, the V_{oc} can be defined as

$$V_{oc} = \frac{\sigma x}{\varepsilon_0} \quad (3)$$

It can be observed from Eq. (3) that the open-circuit voltage (V_{oc}) of the contact-mode TEG increases with the increment of the spacer distance (x) and the inner surface charge density (σ). Considering the porous surface structure and elastic nature of PA6 and PVDF-$ZnSnO_3$ membranes, the increase in the impact force causes a larger interfacial deformation and filling of the vacant pores, leading to a larger effective contact charging area and therefore higher surface charge density (σ) [6,40,41]. Thus, the increment of the contact force and the spacer distance of the PVDF-$ZnSnO_3$/PA6 TEG should both contribute to the enhancement of the V_{oc} which corresponds to the test results in Figs. 5(c) and S5. Furthermore, it was observed that the V_{oc} of the PVDF-$ZnSnO_3$/PA6 TEG did not saturate even when the applied impact force was increased to the magnitude of over 1600 N. Due to its large input detection range and displayed linear relationship, the PVDF-$ZnSnO_3$/PA6 TEGs can be expected to be utilized as pressure, tactile sensors.

It is widely recognized that both PVDF [17, 18, 44] and $ZnSnO_3$ [23, 42, 43, 45] have strong piezoelectric response and thus have been employed previously for energy harvesting applications. The PVDF-$ZnSnO_3$/PA6 TEG was further utilised as an energy harvesting device to drive a series of over 40 LEDs without any charge storage. For this, the contact-separation process of TEG (20 mm spacer distance) was driven by a repetitive compressive force applied by hand. Furthermore, comparison with a PVDF/PA6 TEG with a PVDF film obtained by conventional hot-pressing technique was also carried out to ascertain the effect of phase-inversion and indeed the addition of $ZnSnO_3$ to the PVDF matrix. It was observed that the maximum peak value of output voltage of TEG fabricated by PVDF-$ZnSnO_3$ blend membrane and PA6 was measured to be 222 V and the maximum output voltage of pristine PVDF/PA6 TEG at the same condition was 122 V, while that with the hot-press PVDF membrane was restricted to 30 V only (see supplementary information, S6). While the LEDs could be turned on easily (Figs. 6(a, b)) by pressing of the TEG by hand, it was observed that full brightness could be achieved (Fig. 6(d)) using a 1 μF capacitor which was charged up by repeated pressing of the TEG, in which the voltage developed across the capacitor was dependent on the number of press of the TEG (see Fig. 6(c)).

Now, the significant differences in the hot-pressed and phase-inversion membranes can be discussed in light of the role of rapid quenching and fast solvent-non-solvent interactions. As discussed in our earlier work, fast quenching at low temperatures induces a strong thermal field gradient, causing the crystals to align along the thermal field direction [19]. Furthermore, the possible hydrogen bonding between the C-F group of PVDF with the O-H

group of the water of the PVDF molecule can lead to orientational effects in the resulting membrane [19, 46, 47]. It has been previously observed that during the immersion of the dope solution in a non-solvent bath, the solvent non-solvent mass exchange is rapid, leading to enhanced interfacial polymer concentration. The conformation entropy changes occurring due to this increase in the polymer concentration leads to higher orientation and packing of the CH_2-CF_2 dipoles, leading to the formation of β-phase [24]. Thus, as compared to phase inversion method, the hot-press method in which there is no preferential orientation of the dipoles low, significantly low polarisation is obtained which is reflected in the much lower voltage output of the TEG. This is in line with results obtained by Bai et al. in which the dipole moment in polarised PVDF was tuned to significantly enhance the voltage output from 72 V to 215 V [28]. It was proposed that the presence of bond charges generated by aligned dipoles can influence the potential energy and the resulting surface charge density of the PVDF thin films [28].

3.3 Electric microscopy characterization of membranes

In order to further investigate the electrical charge present in pristine PVDF and PVDF-$ZnSnO_3$ membranes, the electric force microscopy (EFM) experiments were conducted on these samples. Figs. 7(a, b) show the topography, while Figs. 7(c, d) show the representative EFM frequency images of the pristine PVDF and PVDF-$ZnSnO_3$ membranes obtained at a lift height of z = 160 nm. The sample root mean square (r.m.s) roughness observed from topography images was 61 nm and 78 nm for PVDF and PVDF-$ZnSnO_3$ membranes respectively. In EFM, the AFM cantilever scans the surface morphology, followed by a retrace of the trajectory with its resonance frequency f_0 at a fixed height (lift height, z). In the second scan (lift mode), the electrostatic force gradient can be reflected by the cantilever frequency shift, Δf, with respect to its resonance frequency, f_0, [48-50]

$$\Delta f = f - f_0 = -\frac{f_0}{4k}\frac{\partial^2 C}{\partial z^2}\left[(V_{EFM} - V_s)^2 + 2V_Q(V_{EFM} - V_s) + V_Q^2\right] \quad (4)$$

where k is the spring constant of the AFM cantilever, C is the capacitance between the tip and the sample, V_{EFM}, is the bias applied to the tip with respect to the sample, V_s, the surface potential and V_Q the additional surface potential proportional to the stored surface charge Q_i. The sample was grounded, and a bias of 0.5 V was applied to the conducting AFM probe during the lift mode. The frequency shift obtained from the EFM measurements can be

related to the surface charge present on the sample. Higher the frequency shift, greater the surface charge present on the sample. As the tip−sample separation (or lift height, z) increases, Δf decreases due to the weaker electrostatic force gradient in the vertical direction (supporting information, S7). Due to highly inhomogeneous nature of the membranes, the quantification of electric charge is challenging. Nevertheless, qualitatively, from the EFM contrast, we can definitely conclude that a stronger electrostatic signal is detected in case of PVDF-$ZnSnO_3$ as compared to pure PVDF sample. The increase in the triboelectric output may be attributed to the enhanced charge density of PVDF membranes by $ZnSnO_3$.

Figs. 7(e & f) show the PFM amplitude images, while Figs. 7(g & h) represent the PFM phase images of pristine PVDF and PVDF-$ZnSnO_3$ membranes, respectively. The amplitude of the detected piezoelectric signal is related to the piezoelectric coefficient (electromechanical coupling) of the samples, while the phase of the signal can reflect the polarization direction or orientations. From Figs. 7(e & f) and Figs. 7(g & h), it is evident that the piezoresponse contrast (both amplitude and phase signal) is pronounced for PVDF-$ZnSnO_3$ membrane sample as compared to pristine PVDF sample. The vertical piezoresponse was calibrated using deflection sensitivity of the AFM cantilever tip obtained from the force-displacement curve. For more information on the d_{33} measurement procedure, please refer to the supporting information. The calculated piezoelectric coefficient of pristine PVDF membranes was -44 pmV^{-1} while PVDF-$ZnSnO_3$ membranes show a very high piezoelectric coefficient of up to −65 pmV^{-1}. This enhanced piezoelectric effect explains the observed enhancement in triboelectric output voltage of in PVDF-$ZnSnO_3$ membranes as compared to PVDF membranes. It is worth pointing out that further enhancement of the power of PVDF-$ZnSnO_3$/PA6 TEG can be carried out using controlled, patterned micro/nano structuring. This is under investigation, and will be reported elsewhere.

4. Conclusions

In summary, we report high performance, PVDF-$ZnSnO_3$/PA6 TEGs incorporating piezoelectric $ZnSnO_3$ nanocubes. The enhanced polarisation of the PVDF-$ZnSnO_3$ composite membranes leads to a significant increase in the power output wherein the V_{oc} and I_{sc} values were enhanced by approximately 70% and 200% from 300 V to 520 V and from 0.91 mAm^{-2} to 2.7 mAm^{-2}, respectively when subjected to a 489N/3Hz impact frequency. The increase in the electrical output was attributed to the enhanced polarisation of PVDF-$ZnSnO_3$

membranes (-65 pmV^{-1} vs. -44 pmV^{-1} for pristine PVDF) which led to enhanced surface charge density especially at higher applied forces leading to stress induced polarisation and generation of stronger piezoelectric potential. The facile preparation method of phase inversion has several advantages of ease of fabrication, high performance and makes the charge injection step redundant thereby making it an excellent candidate for large scale device fabrication and self-powered systems.

Acknowledgements

Materials support from Solvay Speciality Polymers and William Blythe Ltd. (United Kingdom) is greatly acknowledged. The authors are thankful to Dr V. Parikh at Manchester Metropolitan University for his help in acquiring the EDX data. The authors acknowledge partial financial support by NSFC (61274037).

References

[1] F. Fan, L. Lin, G. Zhu, W. Wu, R. Zhang, Z. L. Wang, Transparent Triboelectric Nanogenerators and Self-Powered Pressure Sensors Based on Micropatterned Plastic Films, Nano Lett. 12 (2012) 3109-3114.

[2] M. Ha, J. Park, Y. Lee, H. Ko, Triboelectric generators and sensors for self-powered wearable electronics, ACS Nano. 9(4) (2015) 3421-3427.

[3] F. R. Fan, Z. Q. Tian, Z. L. Wang, Flexible triboelectric generator, Nano Energy. 1(2) (2012) 328-334.

[4] G. Zhu, B. Peng, J. Chen, Q. Jing, Z. L. Wang, Triboelectric nanogenerators as a new energy technology: From fundamentals, devices, to applications, Nano Energy. 14(2015) 126-138.

[5] L. McCarty, G. Whitesides, Electrostatic Charging Due to Seperation of Ions at Interfaces: Contact Electrification of Ionic Electrets, Angew. Chem. Int. Ed. *47*(12) (2008), 2188-2207

[6] Z. L. Wang, Triboelectric Nanogenerators as New Energy Technology for Self-Powered Systems and as Active Mechanical and Chemical Sensors, ACS Nano. 7 (2013) 9533-9557.

[7] M. Seol, J. Woo, S. Jeon, D. Kim, S. Park, J. Hur, Y. K. Choi, Vertically stacked thin triboelectric nanogenerator for wind energy harvesting, Nano Energy. 14 (2015) 201-208.

[8] Z. Lin, G. Cheng, W. Wu, K. Pradel, Z. L. Wang, Dual-Mode Triboelectric Nanogenerator for Harvesting Water Energy and as a Self-Powered Ethanol Nanosensor, ACS Nano. 8 (2014) 6440-6448.

[9] Z. Wang, L. Cheng, Y. Zheng, Y. Qin, Z. L. Wang, Enhancing the performance of triboelectric nanogenerator through prior-charge injection and its application on self-powered anticorrosion, Nano Energy. 10(2014) 37-43.

[10] Y. Zheng, L. Cheng, M. Yuan, Z. Wang, L. Zhang, Y. Qin, T. Jing, An electrospun nanowire-based triboelectric nanogenerator and its application in a fully self-powered UV detector, Nanoscale. 6 (2014) 7842-7846.

[11] X. Wang, S. Niu, Y. Yin, F. Yi, Z. You, Z. L. Wang, Triboelectric Nanogenerator Based on Fully Enclosed Rolling Spherical Structure for Harvesting Low-Frequency Water Wave Energy, Adv. Energy Mater. 5(24) (2015) 1501467.

[12] H. Y. Li, L. Su, S. Y. Kuang, C. F. Pan, G. Zhu, Z. L. Wang, Significant Enhancement of Triboelectric Charge Density by Fluorinated Surface Modification in Nanoscale for Converting Mechanical Energy, Adv. Func. Mater. 25(35) (2015) 5691-5697.

[13] X. Zhang, M. Han, R. Wang, F. Zhu, Z. Li, W. Wang, H. X. Zhang, Frequency-Multiplication High-Output Triboelectric Nanogenerator for Sustainably Powering Biomedical Microsystems , Nano Lett. 13 (2013) 1168-1172.

[14] G. Zhu, C. Pan, W. Guo, C. Chen, Y. Zhou, R. Yu, Z. L. Wang, Triboelectric-Generator-Driven Pulse Electrodeposition for Micropatterning, Nano Lett. 12 (2012) 4960-4965.

[15] M. Seol, J. Woo, D. Lee, H. Im, J. Hur, Y. Choi, Nature-Replicated Nano-in-Micro Structures for Triboelectric Energy Harvesting, Small. 10 (2014) 3887-3894.

[16] G. Zhu, Z. H. Lin, Q. Jing, P. Bai, C. Pan, Y. Yang, Y. Zhou, Z. L. Wang, Towards large-scale energy harvesting by a nanoparticle-enhanced triboelectric nanogenerator Nano Lett. 13(2) (2013), 847-853.

[17] W. S. Jung, M. G. Kang, H. G. Moon, S. H. Baek, S. J. Yoon, Z. L. Wang, S. W. Kim, C. Y. Kang, High output piezo/triboelectric hybrid generator, Sci. Rep., 5 (2015), 9309.

[18] K. Lee, S. Kim, J. Lee, D. Seol, M. Gupta, Y. Kim, S. W. Kim, Controllable Charge Transfer by Ferroelectric Polarization Mediated Triboelectricity Adv. Funct. Mater. 26 (2016) 3067-3073.

[19] N. Soin, D. Boyer, K. Prashanthi, S. Sharma, A. A. Narasimulu, J. Luo, T. H. Shah, E. Siores, T. Thundat, Exclusive self-aligned β-phase PVDF films with abnormal piezoelectric coefficient prepared via phase inversion, Chem. Commun. 51 (2015) 8257-8260.

[20] Y. Inaguma, D. Sakurai, A. Aimi, M. Yoshida, T. Katsumata, D. Mori, J. Yeon, P. S. Halaysymani, Dielectric properties of a polar ZnSnO3 with LiNbO3-type structure, J. Solid State Chem. 195 (2012) 115-119.

[21] J. Wu, C. Xu, Y. Zhang, Z. L. Wang, Lead-Free Nanogenerator Made from Single $ZnSnO_3$ Microbelt, ACS Nano. 6 (2012) 4335-4340.

[22] D. Kovacheva, Preparation of crystalline ZnSnO3 from Li2SnO3 by low-temperature ion exchange, Solid State Ionics. 109 (1998) 327-332.

[23] G. Wang, Y. Xi, H. Xuan, R. Liu, X. Chen, L. Cheng, Hybrid nanogenerators based on triboelectrification of a dielectric composite made of lead-free ZnSnO3 nanocubes, Nano Energy. 18 (2015) 28-36.

[24] M. Zhang, A. Zhang, B. Zhu, C. Du, Y. Xu, Polymorphism in porous poly(vinylidene fluoride) membranes formed via immersion precipitation process, J. Membr. Sci. 319 (2008) 169-175.

[25] X. Li, Y. Wang, X. Lu, C. Xiao, Morphology changes of polyvinylidene fluoride membrane under different phase separation mechanisms, J. Membr. Sci., 320 (2008) 477-482.

[26] D. J. Lin, C. L. Chang, C. K. Lee, L. P. Cheng, Fine structure and crystallinity of porous Nylon 66 membranes prepared by phase inversion in the water/formic acid/Nylon 66 system, Eur. Polym. J. 42(2) (2006) 356-367.

[27] L. P. Cheng, D. J. Lin, K. C. Yang, Formation of mica-intercalated Nylon-6 nanocomposite membranes by phase inversion, J. Membr. Sci. 172 (2000) 157-166.

[28] P. Bai, G. Zhu, Y. Zhou, S. Wang, J. Ma, G. Zhang, Z. L. Wang, Dipole-moment-induced effect on contact electrification for triboelectric nanogenerators, Nano Res. 7 (2014) 990-997.

[29] J. Chen, H. Guo, X. He, G. Liu, Y. Xi, H. Shi, C. Hu, Enhancing performance of triboelectric nanogenerator by filling high dielectric nanoparticles into sponge PDMS film, ACS Appl. Mater. Interfaces. 8(1) (2015) 736-744.

[30] C. Tsonos, C. Pandis, N. Soin, D. Sakellari, E. Myrovali, S. Kripotou, A. Kanapitsas, E. Siores, Multifunctional nanocomposites of poly (vinylidene fluoride) reinforced by carbon nanotubes and magnetite nanoparticles, Exp. Poly. Lett. 9(12) (2015) 1104-1118.

[31] R. Gregorio, Determination of the α, β, and γ crystalline phases of poly(vinylidene fluoride) films prepared at different conditions, J. Appl. Polym. Sci. 100 (2006) 3272-3279.

[32] S. Lanceros-Méndez, J. Mano, A. Costa, V. Schmidt, FTIR and DSC studies of mechanically deformed β-PVDF films, J. Macromol. Sci. B. 40 (2001) 517-527.

[33] J. Gomes, J. Serrado Nunes, V. Sencadas, S. Lanceros-Mendez, Influence of the β-phase content and degree of crystallinity on the piezo- and ferroelectric properties of poly(vinylidene fluoride), Smart Mater. Struct. 19 (2010) 065010.

[34] N. Soin, T. Shah, S. Anand, J. Geng, W. Pornwannachai, P. Mandal, D. Reid, S. Sharma, R. L. Hadimani, D. V. Bayramol, E. Siores, Novel "3-D spacer" all fibre piezoelectric textiles for energy harvesting applications, Energy Environ. Sci. 7(5) (2014) 1670-1679.

[35] P. Martins, A. Lopes, S. Lanceros-Mendez, Electroactive phases of poly(vinylidene fluoride): Determination, processing and applications, Prog. Polym. Sci. 39 (2014) 683-706.

[36] B. E. Mohajir, N. Heymans, Changes in structural and mechanical behaviour of PVDF with processing and thermomechanical treatments. 1. Change in structure, Polymer, 42 (2001) 5661-5667.

[37] S. Jana, S. Garain, S. Sen, D. Mandal, The influence of hydrogen bonding on the dielectric constant and the piezoelectric energy harvesting performance of hydrated metal salt mediated PVDF films, Phys. Chem. Chem. Phys. 17 (2015) 17429-17436.

[38] D. Mandal, K. Henkel and D. Schmeißer, Improved performance of a polymer nanogenerator based on silver nanoparticles doped electrospun P(VDF–HFP) nanofibers, Phys. Chem. Chem. Phys. 16 (2014) 10403–10407.

[39] P. Nallasamy, S. Mohan, Vibrational spectroscopic characterization of form II poly (vinylidene fluoride), Indian J. Pure Appl. Phys. 43. 11 (2005) 821-827.

[40] S. Niu, S. Wang, L. Lin, Y. Liu, Y. Zhou, Y. Hu, Z. L. Wang, Theoretical study of contact-mode triboelectric nanogenerators as an effective power source, Energy Environ. Sci. 6 (2013) 3576-3583.

[41] M. Taghavi, L. Beccai, A contact-key triboelectric nanogenerator: Theoretical and experimental study on motion speed influence, Nano Energy. 18 (2015) 283-292.

[42] K. Lee, D. Kim, J. Lee, T. Kim, M. Gupta, S. Kim, Hybrid Nanocomposites: Unidirectional High-Power Generation via Stress-Induced Dipole Alignment from ZnSnO 3 Nanocubes/Polymer Hybrid Piezoelectric Nanogenerator, Adv. Funct. Mater. 24 (1) (2014) 37-43.

[43] M. Alam, S. Ghosh, A. Sultana, D. Mandal, Lead-free ZnSnO3/MWCNTs-based self-poled flexible hybrid nanogenerator for piezoelectric power generation, Nanotechnology 26 (2015) 165403.

[44] S. Cha, S. M. Kim, H. Kim, J. Ku, J. I. Sohn, Y. J. Park, B. G. Song, M. H. Jung, E. K. Lee, B. L. Choi, J. J. Park, Porous PVDF As Effective Sonic Wave Driven Nanogenerators, Nano Lett. 11 (2011) 5142-5147.

[45] J. Wu, C. Xu, Y. Zhang, Y. Yang, Y. Zhou, Z. L. Wang, Flexible and Transparent Nanogenerators Based on a Composite of Lead-Free ZnSnO3 Triangular-Belts, Adv. Mater. 24 (2012) 6094-6099.

[46] S. Chen, X. Li, K. Yao, F. E. H. Tay, A. Kumar, K. Zeng, Self-polarized ferroelectric PVDF homopolymer ultra-thin films derived from Langmuir–Blodgett deposition, Polymer. 53 (6) (2012) 1404-1408.

[47] B. J. Rodriguez, S. Jesse, S. V. Kalinin, J. Kim, S. Ducharme, V. M. Fridkin, Nanoscale polarization manipulation and imaging in ferroelectric Langmuir-Blodgett polymer films, Appl. Phys. Lett. 90 (2007) 122904.

[48] D. M. Schaadt, E. T. Yu, S. Sankar A. E. Berkowitz, Charge Storage in Co nanoclusters embedded in SiO2 by scanning force microscopy, Appl. Phys. Lett. 74(1999) 472-474.

[49] P. M. Bridger, Z. Z. Bandic, E. C. Piquette, T. C. McGill, Measurement of induced surface charges, contact potentials, and surface states in GaN by electric force microscopy, Appl. Phys. Lett. 74(1999) 3522-3524.

[50] Y. Martin, D. W. Abraham, H. K. Wickramasinghe, High-resolution capacitance measurement and potentiometry by force microscopy, Appl. Phys. Lett., 52 (1988)1103-1105.

Figures

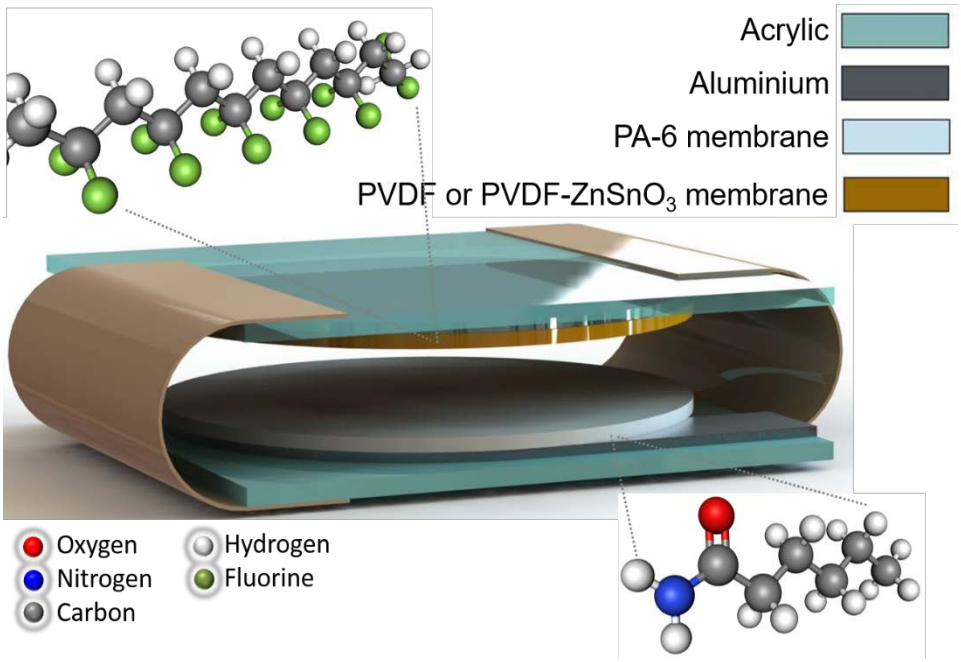

Figure 1. Structure of the TEG showing the position of the various components

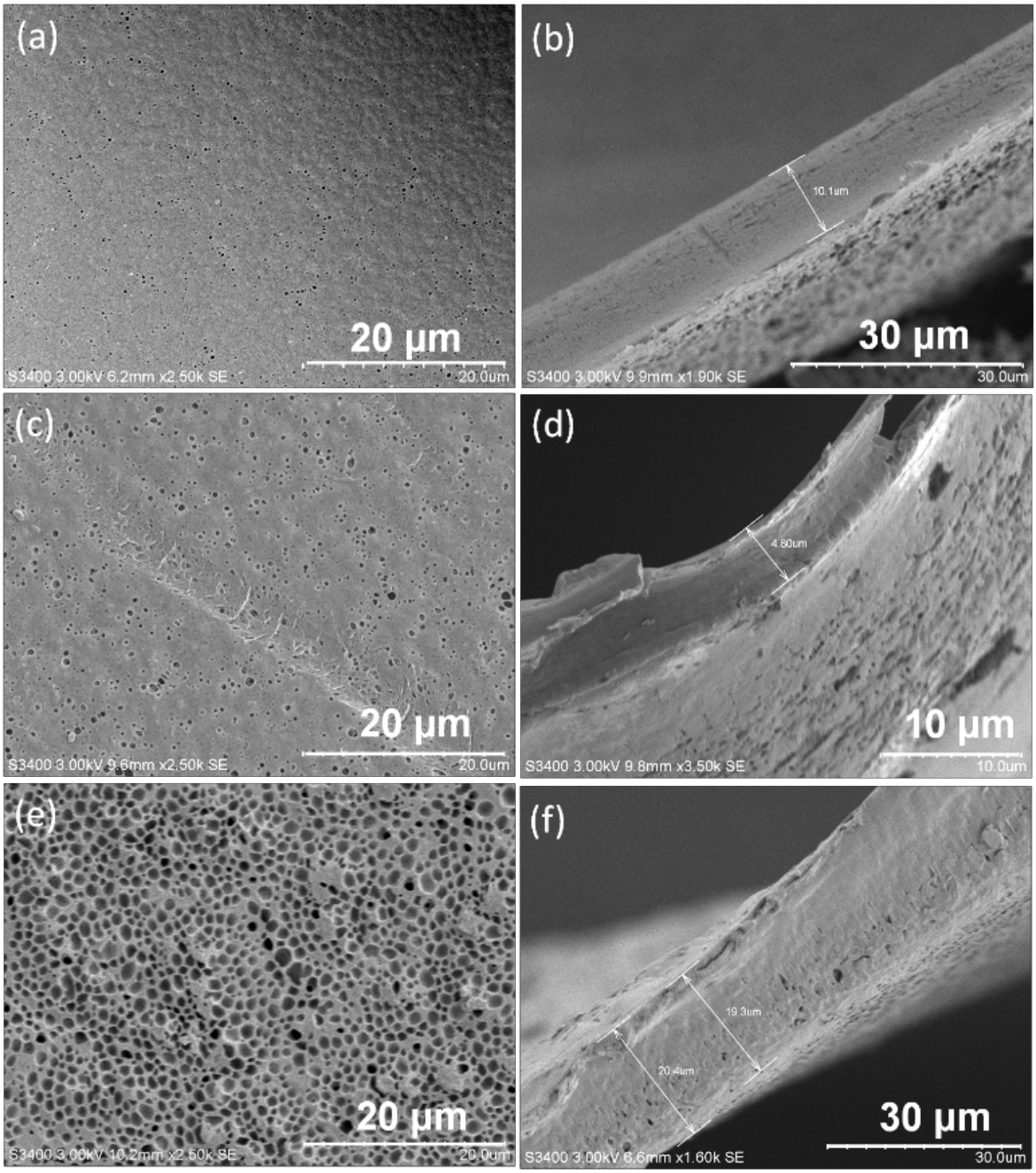

Figure 2. Scanning electron microscopy images of the surface and thickness cross-section of (a, b) pristine PVDF membrane, (c, d) PVDF-$ZnSnO_3$ membrane and (e, f) PA6 membrane.

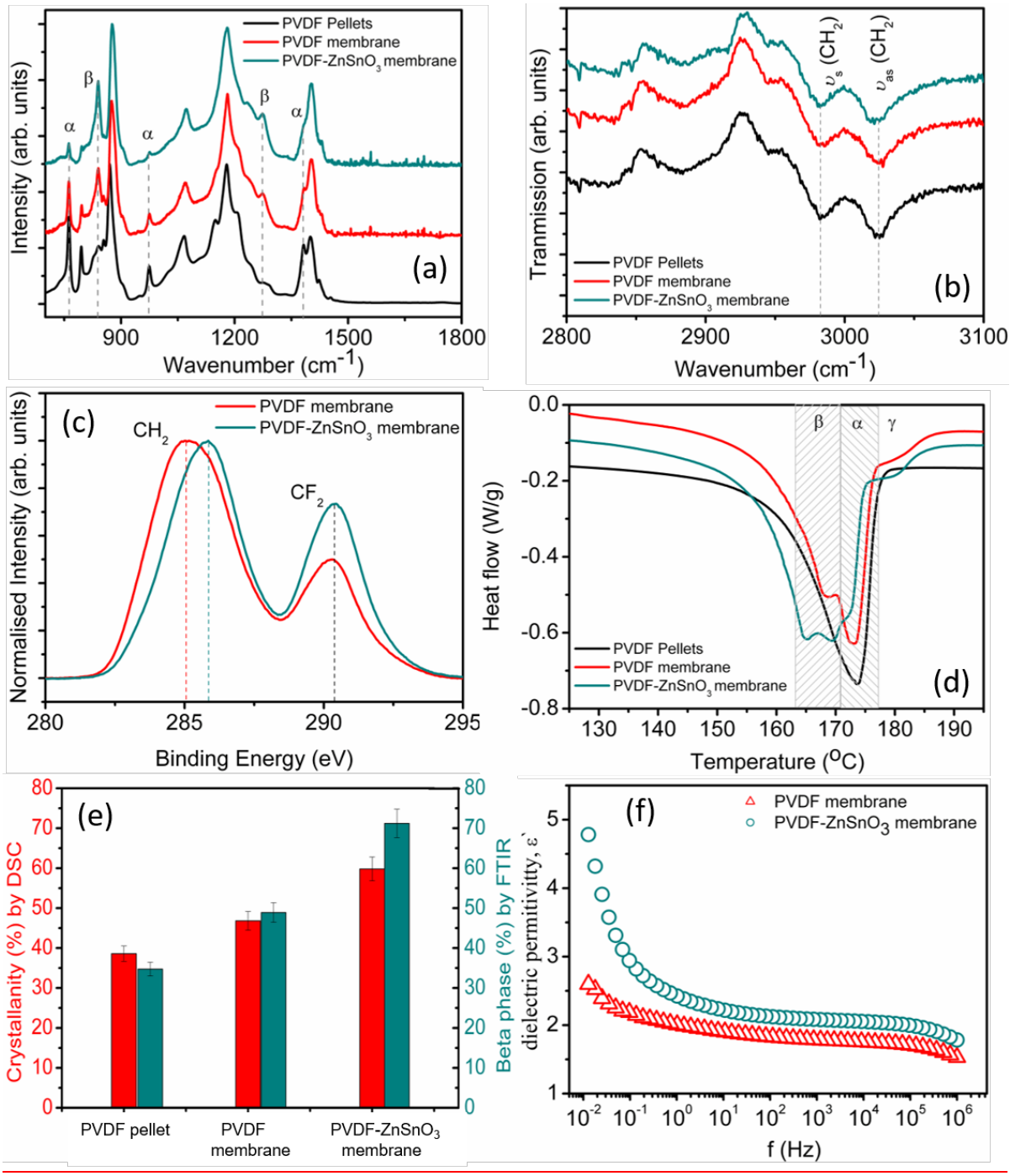

Figure 3. (a) FTIR spectra of pristine PVDF and PVDF-$ZnSnO_3$ membranes, the comparative spectra of the starting PVDF pellets is also shown for comparison, (b) transmission FTIR spectra showing the shifts in the CH_2 symmetric and asymmetric modes, (c) C1s core level XPS spectra confirming the interactions between $ZnSnO_3$ and PVDF, (d) DSC spectra of PVDF pellets, pristine PVDF membrane and PVDF-$ZnSnO_3$ membrane showing the lowering of melting temperature for membranes, (e) corresponding increase in the β-phase upon addition of $ZnSnO_3$ to PVDF can be clearly observed in the enhanced crystallinity as well as β-phase, (f) variation of dielectric behaviour of the PVDF and PVDF-$ZnSnO_3$ membranes as a function of frequency.

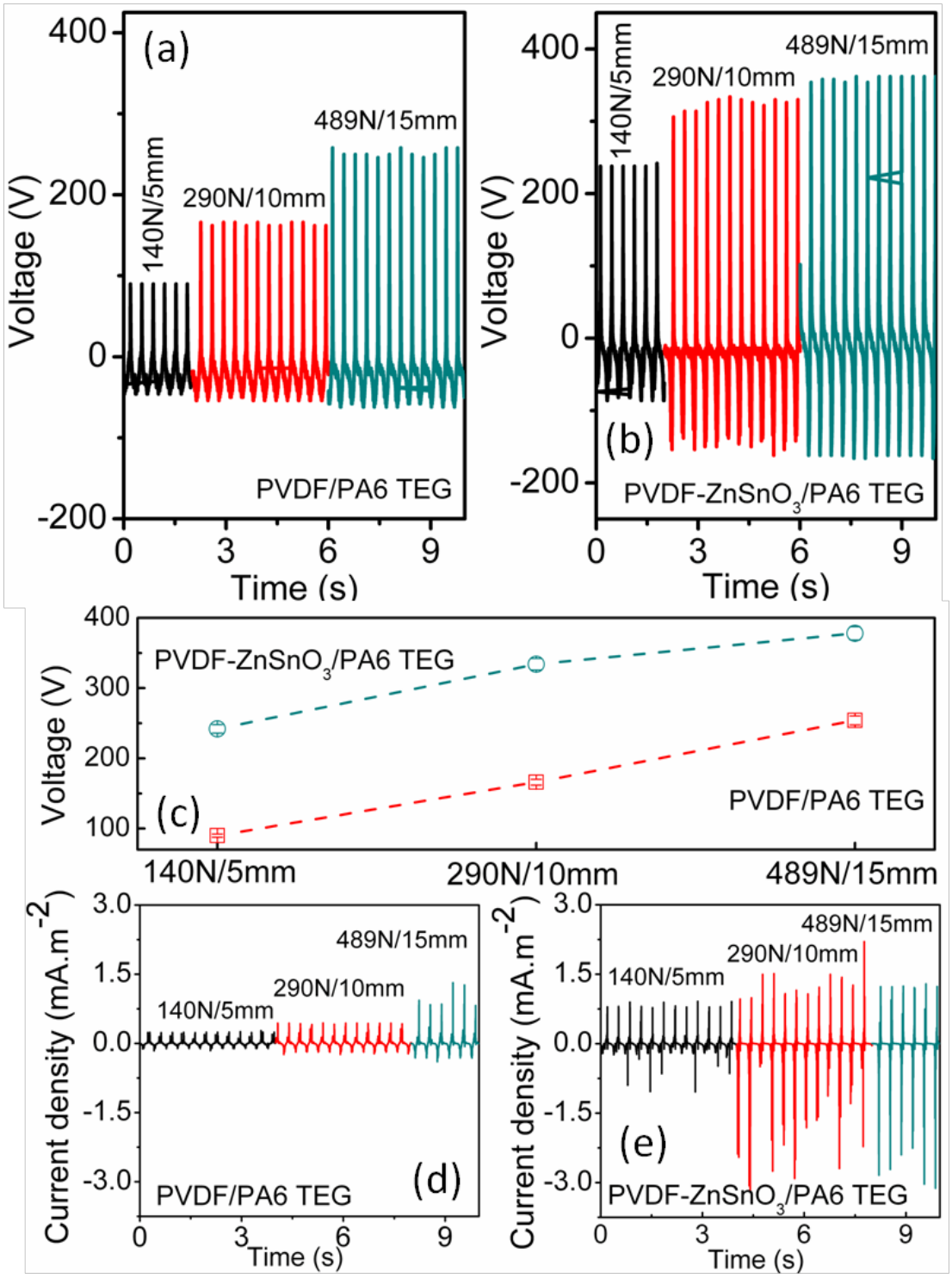

Figure 4. Open circuit voltage (V_{oc}) values of the TEGs to a 3 Hz working frequency with three different spacer values and impact force for (a) PVDF/PA6 TEG and (b) PVDF-$ZnSnO_3$/PA6 TEG; (c) differences between the peak V_{oc} for the two TEGs; corresponding short circuit current values for (d) PVDF/PA6 TEG and (e) PVDF-$ZnSnO_3$/PA6 TEG.

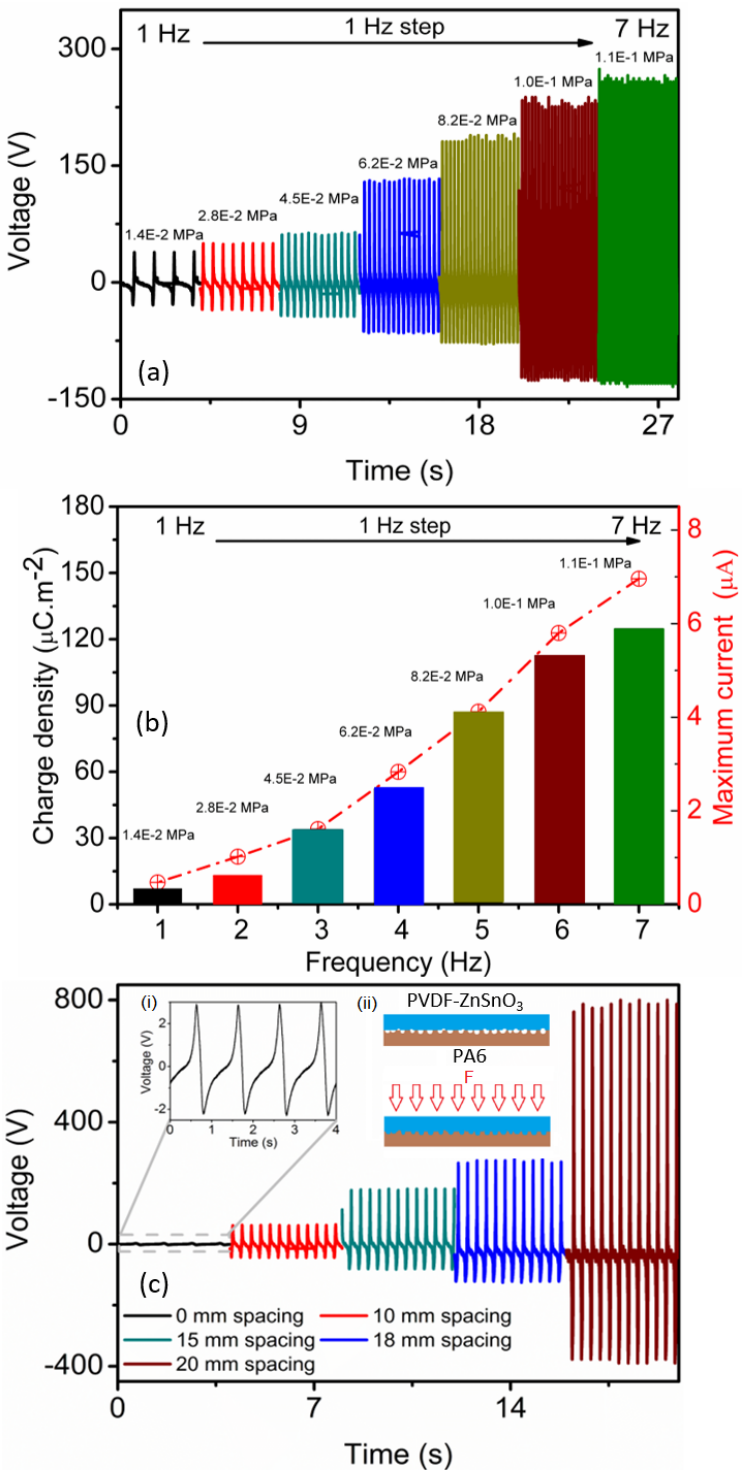

Figure 5. Measured V_{oc} values of the PVDF-$ZnSnO_3$/PA6 TEGs at frequency range from 1 Hz to 7 Hz with the corresponding applied pressure (space distance of 10 mm), (b) variation of maximum short circuit current and corresponding charge density a frequency range from 1-7 Hz, (c) effect of spacer distance on the V_{oc} values of the PVDF-$ZnSnO_3$/PA6 TEG with the inset showing (i) the waveform and (ii) the change of interface of the membranes when external force applied on the TEG without any spacer (3 Hz).

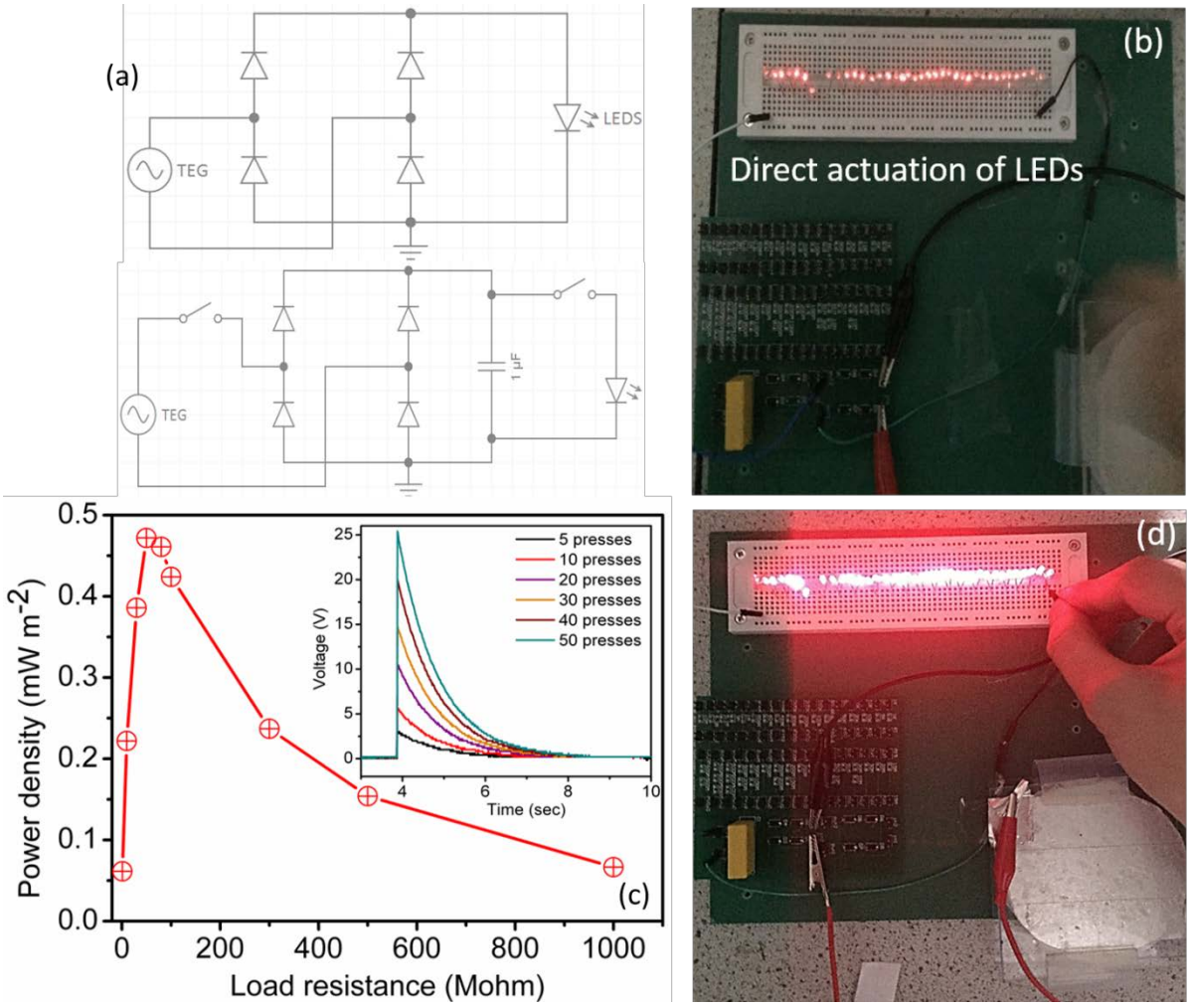

Figure 6: (a) Circuit schematics for the direct actuation and incorporating a charge storage capacitor utilising the PVDF-$ZnSnO_3$/PA6 TEG as energy harvesting element, (b) direct powering of the LEDs obtained by pressing of the PVDF-$ZnSnO_3$/PA6 TEG by hand, (c) power density vs. load curve showing the maximum power of 0.47 mWm^{-2} at a load of 50 MΩ with the inset showing the discharging curves and capacitor voltages on the 1 µF capacitor charged by PVDF-$ZnSnO_3$/PA6 TEG pressed by hand, (d) full brightness achieved for the LEDs via the discharge of the 1 µF capacitor.

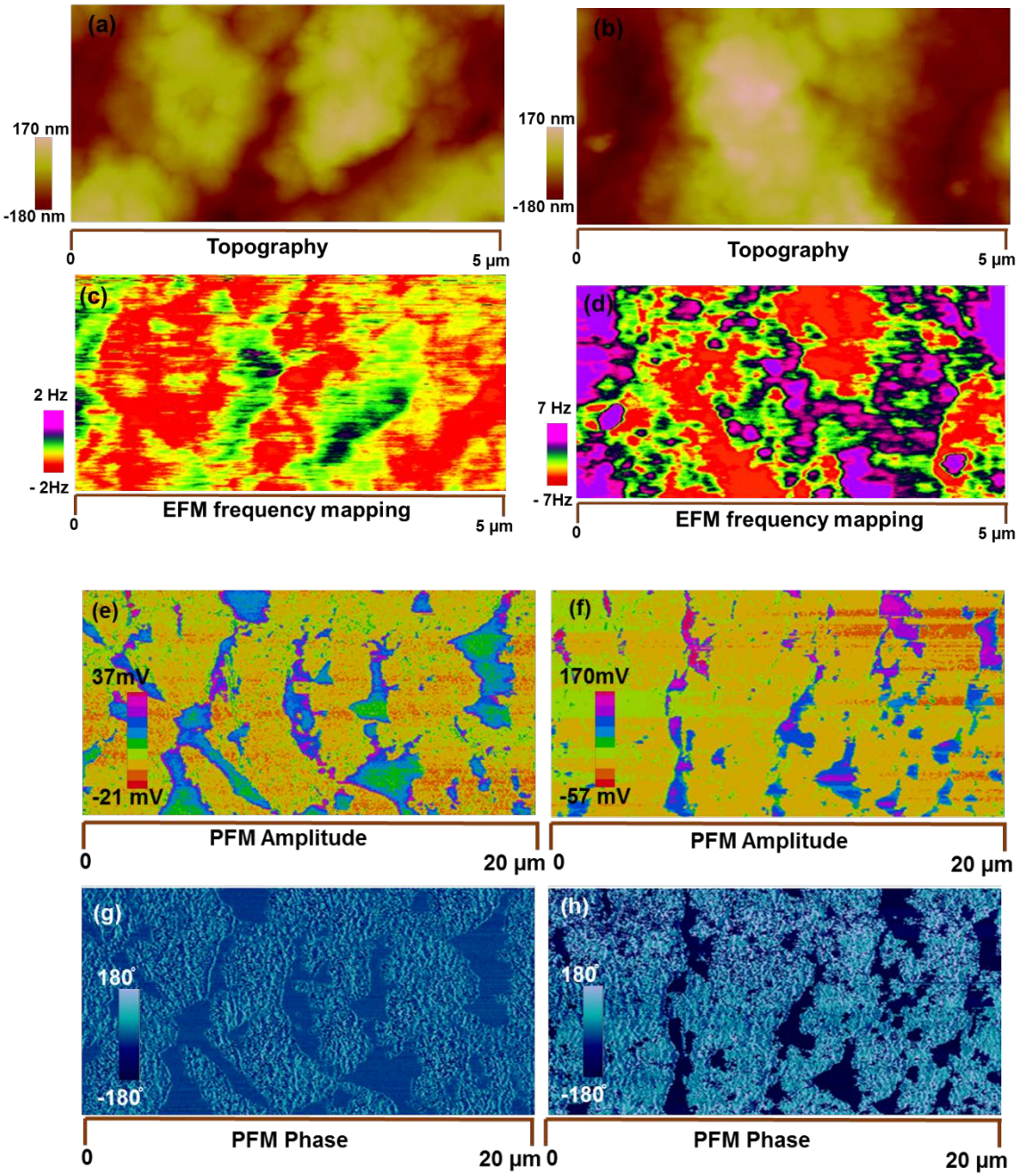

Figure 7: (a & b) Topography images of pristine PVDF and PVDF-$ZnSnO_3$ membranes respectively, (c & d) EFM frequency mapping of pristine PVDF and PVDF-$ZnSnO_3$ membranes showing electric field gradient distribution in the samples. During interleave mode, the lift height used was 160 nm. (e & f) PFM amplitude images of pristine PVDF and PVDF-$ZnSnO_3$ membranes respectively, (g & h) PFM phase images of pristine PVDF and PVDF-$ZnSnO_3$ membranes respectively.